Check for updates

Liquid-assisted grinding/compression: a facile mechanosynthetic route for the production of high-performing Co–N–C electrocatalyst materials†

Akmal Kosimov,[a] Gulnara Yusibova,[a] Jaan Aruväli,[b] Päärn Paiste,[b] Maike Käärik,[a] Jaan Leis,[a] Arvo Kikas,[c] Vambola Kisand,[c] Krišjānis Šmits[d] and Nadezda Kongi [ID] *[a]

Worldwide implementation of energy conversion devices such as metal–air batteries and fuel cells needs an innovative approach for the sustainable design of noble metal-free electrocatalysts. A key factor to be considered is the industry-scale production method, which should be cost and energy-effective, and environmentally friendly. A novel solid-phase-based methodology is introduced herein as a new approach for the mechanosynthesis of M–N–C-type catalysts. This method employs low-cost commercially available materials, is time and energy-efficient, results in no solvent/toxic waste and does not require a complex post-synthetic treatment. The liquid-assisted grinding/compression approach yielded a series of meso- and microporous Co–N–C catalysts, with excellent bifunctional activity towards oxygen evolution and reduction reactions. In-depth physical characterization confirmed that all NaCl-supported catalysts possess cross-linked sheet-like mesoporous carbon structures with high exposure of catalytically active sites. This study provides a new avenue for the large-scale production of high-performance and low-cost M–N–C materials *via* energy-effective and environmentally sustainable synthetic protocols.

Introduction

In recent years, fuel cells, metal–air batteries, and water electrolysers have been striking as excellent alternative energy conversion and storage devices.[1] However, the performance of these systems depends on sluggish kinetics of the key electrochemical processes – oxygen reduction reaction (ORR), oxygen evolution reaction (OER), and hydrogen evolution reaction (HER), which determine their overall performance and significantly impede the advancements of these energy systems. Nevertheless, despite the drawbacks, electrochemical energy devices, with their zero-emission operation, promise to be a good candidate for replacing fossil fuel-based energy processes.[2,3]

One of the key limiting factors for the commercialization of fuel-cells and metal–air batteries is the relatively high cost caused by the use of platinum group metals (PGMs), which are applied to effectively overcome the ORR/OER overpotentials.[4,5] Despite the advances in decreasing their cost, the PGM-based catalyst still constitutes the major part of the fuel-cell/metal–air battery price.[6] Thus, it is necessary to find a replacement for noble-metal-based catalysts to make these energy systems more accessible for widespread applications.

Among the recently developed non-noble-metal-based materials, transition metal–nitrogen-doped carbon (M–N–C) materials demonstrate catalytic activity comparable with commercially available catalysts.[7,8] Their low cost and a wide variety of sources make them excellent candidates for replacing Pt-based catalysts.[9–13] ORR electroactivity of M–N–C materials is often attributed to various single-atom sites, where metal is coordinated to nitrogen (M–N_x), whereas OER activity is generally enhanced by a presence of nanoparticles in pure metallic form.[14–18] Furthermore, to improve catalytic efficiency, access to the catalytically active sites should also be ensured by increasing the porosity of the carbon materials. Thus, recent advances in this field involved the application of templating agents, which, upon their removal, are expected to leave vacant pores and enhance the porosity.[19–21] As the templated catalyst precursor materials usually object to carbonization, the templating agent should withstand elevated temperatures. Hence preference is given to cheap and environmen-

[a]*Institute of Chemistry, University of Tartu, Tartu 50411, Estonia.*
E-mail: nadezda.kongi@ut.ee
[b]*Institute of Ecology and Earth Sciences, University of Tartu, Tartu 50411, Estonia*
[c]*Institute of Physics, University of Tartu, Tartu 50411, Estonia*
[d]*Institute of Solid State Physics, University of Latvia, LV-1063 Riga, Latvia*
†Electronic supplementary information (ESI) available. See DOI: 10.1039/d1gc03433b

tally sustainable inorganic sacrificial templates such as (SiO_2, MgO, Mg(OH)$_2$, NaCl).[22–26] Efficiency of the template-assisted method was proven by recent studies, which show that the resulting catalysts exhibited greater catalytic activity compared to their non-templated analogs.[23,26,27]

Despite the extensive research in this field, fabrication of M–N–C materials heavily relies on solvent-based techniques (precipitation, deposition–precipitation, hydrothermal treatments, and impregnation), which are considered from the industrial perspective laborious and complex, and unsustainable to scale up.[28] On the other hand, solid-phase synthetic protocols are gaining traction as green and facile alternatives to solution-based methods.[29,30] Mechanochemistry, where kinetic force is utilized in the form of ball milling (grinding) or compression, is becoming a major method for fabricating various materials.[31–33] Recent examples of mechanochemistry in the domain of materials include the synthesis of MOFs,[31–33] nanoparticles,[34] organic molecules,[35] etc. Moreover, mechanosynthesis possesses numerous attractive hallmarks such as more straightforward, easy-to-scale, and affordable techniques, reduced formation of hazardous substances, and minimized energy requirement, which is considered advantageous from an industrial point of view.[36,37] Nevertheless, to the best of our knowledge, there were hardly any attempts to study mechanochemical reactions to produce M–N–C-type materials. Therefore, our research aimed to develop an optimal mechanosynthetic protocol to improve the fabrication efficiency of M–N–C materials.

Herein, we report a liquid-assisted grinding/compression strategy to produce a highly active and stable bifunctional Co–N–C catalyst using green and cost-effective template-assisted mechanochemistry techniques. The electrocatalytic behavior of produced materials is comparable with commercially available ones, and our original mechanosynthetic protocols have the potential to become a stepping stone to industrial manufacturing of PGM-free catalysts.

Experimental section

General

Tripyridyl triazine (TPTZ) (≥98%) and Co(NO$_3$)$_2$·6H$_2$O were purchased from Aldrich and used as received. MilliQ water was used to prepare all solutions. NaCl crystals were pulverized in a ball mill to achieve an average crystallite size of 10–50 μm. Milling was conducted in a ball mill (Fritsch Planetary Mill Pulverisette 7) using 12 mL zirconium oxide grinding bowls and 5 mm diameter zirconium oxide milling balls. Furnace (Carbolite Gero EST 12/300B) was used for the carbonization of catalyst precursors.

Template-assisted mechanosynthesis of Co–N–C catalysts

The green mechanosynthesis method for producing the series of Co–N–C catalysts is schematically depicted in Fig. 1 and described in details below. For the synthesis of catalyst precursors, liquid-assisted grinding and compression (LAG and LAC) methods and their combinations were applied.
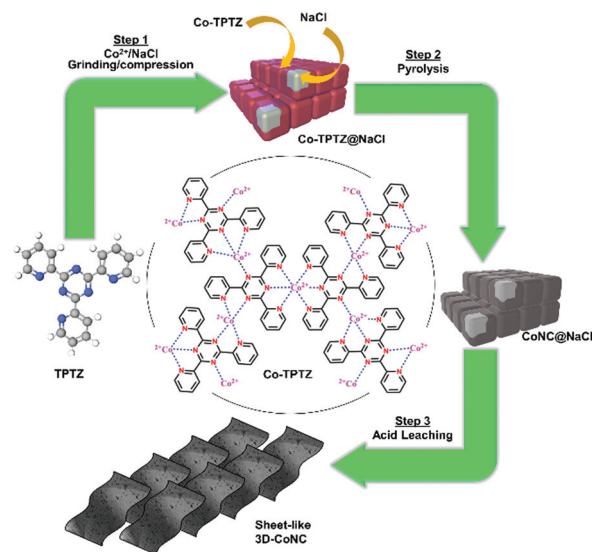

Fig. 1 Schematic diagram of green mechanochemical approach toward synthesis of Co–N–C-type catalysts.

CoNC-LAG. To synthesize the cobalt 2,4,6-tri(2-pyridyl)-1,3,5-triazine complex (Co-TPTZ), Co(NO$_3$)$_2$·6H$_2$O (31 mg, 0.106 mmol, 1 eq.) and 2,4,6-tri(2-pyridyl)-1,3,5-triazine (100 mg, 0.32 mmol, 3 eq.) and 40 μl of EtOH were placed in a ball mill jar and ground at 600 rpm for 20 min. Consequently, the heat-treatment was conducted under a nitrogen atmosphere at 700 °C for 2 h with ramping of 20 °C min^{-1}. To remove the oxide/metal particles, the material was treated with 5 ml of 1 M HCl for 3 h at 70 °C to give **CoNC-LAG** (m = 24.6 mg).

3D-CoNC-LAG. Co(NO$_3$)$_2$·6H$_2$O (31 mg, 0.106 mmol, 1 eq.) and 2,4,6-tri(2-pyridyl)-1,3,5-triazine (100 mg, 0.32 mmol, 3 eq.), NaCl (1 g) and 40 μl of EtOH were placed in a ball mill jar and ground at 600 rpm for 20 min. The heat-treatment was conducted under a nitrogen atmosphere at 700 °C for 2 h with ramping of 20 °C min^{-1}. NaCl was removed by stirring in MilliQ water for 1 h at r.t. The material was filtered off and treated with 5 ml of 1 M HCl for 3 h at 70 °C to give **CoNC@NaCl-LAG** (m = 28.8 mg).

3D-CoNC-LAC. Co(NO$_3$)$_2$·6H$_2$O (31 mg, 0.106 mmol, 1 eq.) and 2,4,6-tri(2-pyridyl)-1,3,5-triazine (100 mg, 0.32 mmol, 3 eq.) and NaCl (1 g) were mixed thoroughly together, placed in a pellet mold, and 40 μl of EtOH was added and compressed at 300 kg cm^{-2} for 10 minutes. The heat-treatment was conducted under a nitrogen atmosphere at 700 °C for 2 h with ramping of 20 °C min^{-1}. NaCl was removed by stirring in MilliQ water for 1 h at r.t. The material was filtered off and treated with 5 ml of 1 M HCl for 3 h at 70 °C to give **3D-CoCN-LAC** (m = 32 mg).

3D-CoNC-LAG-LAC. Co(NO$_3$)$_2$·6H$_2$O (31 mg, 0.106 mmol, 1 eq.) and 2,4,6-tri(2-pyridyl)-1,3,5-triazine (100 mg, 0.32 mmol, 3 eq.), NaCl (1 g) and 40 μl of EtOH were placed in a ball mill jar and ground at 600 rpm for 20 min. The powder was then placed in a pellet mold, EtOH was added and the mixture was

compressed at 300 kg cm^{-2}. The heat-treatment was conducted under a nitrogen atmosphere at 700 °C for 2 h with ramping of 20 °C min^{-1}. NaCl was removed by stirring in MilliQ water for 1 h at r.t. The material was filtered off and treated with 5 ml of 1 M HCl solution leaching for 3 h at 70 °C to give **3D-CoNC-LAG-LAC** (m = 34.1 mg).

Physical characterization

N$_2$ physisorption. Low-temperature nitrogen adsorption was done at the boiling temperature of nitrogen (77 K) by using the NovaTouch LX2 (Quantachrome Instruments). The materials were vacuum dried for 12 h at 300 °C before the measurement. Specific surface area (S_{BET}) of carbon samples was calculated from N$_2$ adsorption corresponding to the Brunauer–Emmett–Teller (BET) theory in the P/P_0 interval of 0.02–0.2. The average pore size was calculated assuming a slit-type pore geometry using the following formula APS = $2V_{tot}/S_{BET}$. Pore size distribution (PSD) was calculated according to the quenched solid density functional theory (QSDFT) equilibrium model for slit-type pores. All calculations were done with TouchWin 1.11 software (Quantachrome Instruments).

X-ray photoelectron spectroscopy (XPS). XPS was conducted at ultra-high vacuum conditions using a non-monochromatic twin anode X-ray tube (Thermo XR3E2) with the characteristic energy of 1253.6 eV (Mg K$_\alpha$) and an electron energy analyzer SCIENTA SES 100. Samples were prepared by deposition of suspension of the catalytic materials in isopropanol at a concentration of 4 mg mL^{-1} onto GC plates (1.1 × 1.1 cm). The survey scan was collected using the energy range from 900 to 0 eV, pass energy of 200 eV, step size of 0.5 eV, step duration 0.2 s, and a number of scans 5. High-resolution XPS scans were performed using pass energy 200 eV and step size 0.1 eV. An Ag wire attached to the sample holders was used for energy reference (Ag 3d5/2 at 367.8 eV); no charging effects were observed. Peak fitting was done using CasaXPS (version 2.3.16) software. For peak fitting, Gauss–Lorentz hybrid function (GL 70, Gauss 30%, Lorentz 70%) and a blend of linear and Shirley-type backgrounds were used.

Powder X-ray diffraction (PXRD). The powder samples were studied by XRD using the Bruker D8 Advance diffractometer with Ni-filtered CuKα radiation, 0.3° divergence slit, two 2.5° Soller slits, and LynxEye line detector. Scanning steps of 0.013°2θ from 5 to 77°2θ and a total counting time of 174 s per step were used.

Microwave plasma-atomic emission spectroscopy (MP-AES). The transition metal concentration in the catalyst materials was determined using MP-AES. 10 mg of sample material was dissolved with the Anton Paar Multiwave PRO microwave digestion system in NXF100 vessels (PTFE/TFM liner) using a mixture of 4 mL of HNO$_3$ and 2 mL of H$_2$O$_2$. Samples were digested at 230 °C and pressures between 45 and 50 bar. After dissolution, the samples were diluted with 2% HNO$_3$ solution to obtain metal concentrations of around 5 mg L^{-1} and analyzed using Agilent 4210 MP-AES at analytical wavelengths Fe 371.993 nm and Co 340.512 nm.

Transition and scanning electron microscopy (TEM and SEM). The morphology of nanoparticles and carbon-based structures was examined by high-resolution SEM-FIB electron microscope Helios 5 UX (FEI-Thermo Scientific) operated at 30 kV using STEM 3+ BF and HAADF detectors. The crystal structure, size verification, and morphology studies of carbon-based structures were performed using a transmission electron microscope Tecnai F20, (FEI) operated at 200 kV. For SEM, TEM samples were transferred to the holey carbon film grid S147-4 (Agar Scientific).

Electrochemical characterization

All electrochemical measurements were carried out in a five-neck electrochemical cell. A reversible hydrogen electrode (RHE) served as a reference electrode and glassy carbon (GC) rod as a counter electrode. Potentials were applied using Autolab PGSTAT128N potentiostat/galvanostat (Metrohm Autolab B.V., The Netherlands), controlled by Nova 2.1.4 software. Rotating disk electrode (RDE) measurements were carried out by OrigaTrod rotating disk electrode linked to OrigaBox speed controller. The electrolyte solution was prepared by dissolving KOH pellets (purity ≥85%, Sigma-Aldrich) in Milli-Q water, and obtained 0.1 M KOH solution was saturated with pure O$_2$ (99.999%, Linde Gas) and deaerated with Ar gas (99.999%, Linde Gas) prior ORR/OER experiments.

Before modification, GC disk electrodes (OrigaTip GC disks with a diameter of 5 mm) were polished to a mirror finish with alumina slurries (1 and 0.3 μm, Buehler). They were sonicated in both isopropanol and Milli-Q water for 5 min to clean polishing residue. The catalyst suspension was prepared by mixing 5 mg of catalyst powder, 5 μl of Nafion ionomer solution (5 wt%, Sigma-Aldrich), and 495 μl of 2-propanol and homogenized by sonication for 1 hour. The catalyst ink was deposited onto a clean GC surface to yield a catalyst loading of 0.5 mg cm^{-2}. The ORR measurements were performed in O$_2$ saturated KOH solution (0.1 M) at a scan rate of 10 mV s^{-1} and at various electrode rotation speeds. The RDE data was analyzed by the Koutecky–Levich (K–L) equation:[32]

$$\frac{1}{j} = \frac{1}{j_k} + \frac{1}{j_d} = -\frac{1}{nFkC_{O_2}^b} - \frac{1}{0.62nFD_{O_2}^{\frac{2}{3}}\nu^{-\frac{1}{6}}C_{O_2}^b\omega^{\frac{1}{2}}}$$

where j, j_k, and j_d denote the measured, kinetic, and diffusion-limited current densities, respectively. F is the Faraday constant (96 485 C mol^{-1}), and n is the number of electrons transferred per oxygen molecule. k is the electrochemical rate constant for O$_2$ reduction, $C_{O_2}^b$ is the concentration of O$_2$ (1.22 × 10^{-6} mol cm^{-3} in 0.1 M KOH),[33] while D_{O_2} shows the diffusion coefficient of O$_2$ (1.93 × 10^{-5} cm^2 s^{-1} in 0.1 M KOH),[33] ω represents the rotation rate of the electrode (rad s^{-1}), and ν is the kinematic viscosity of the solution (0.01 cm^2 s^{-1}).[34]

The OER performances of the as-prepared Co–N–C materials were investigated in a 0.1 M KOH solution with a scan rate of 10 mV s^{-1}. The ORR/OER durability was investigated by a chronoamperometry technique in 0.1 M O$_2$/Ar-saturated KOH electrolyte at a constant potential of 0.6/1.6 V *vs.*

RHE and the current response collected against time over a period of 30 000 s was recorded at an electrode rotation speed of 1600 rpm. An iR correction was applied to all initial electrochemical data.

Results

The synthesis of M–N–C catalysts often employs organic molecules to ensure sufficient carbon and nitrogen content in the catalyst matrix.[15,16,38,39] In this work, 2,4,6-tris(2-pyridyl)-1,3,5-triazine (TPTZ) was implemented both as C/N-source and complexation agent to coordinate towards Co_2^+ ions and form the Co-TPTZ complex. Recent reports show that using Co-TPTZ precursor is beneficial for good catalytic activity, which is assigned to the effective formation of Co–N_x species. Moreover, coordinative bonding between the organic molecules stabilizes Co-ions and inhibits their agglomeration during pyrolysis.[24] Additionally, the NaCl-template-assisted approach was implemented in this work, which was reported to effectively stabilize Co-TPTZ-complex during heat treatment, increase the accessibility of catalytically active sites, and improve porosity.[24] Moreover, NaCl crystallites act as a grinding aid, facilitating the milling, improving materials dispersion, and providing finer particles and narrower particle size distribution.[40] Previously described template-assisted procedures provide highly active catalysts, however these methodologies implement solvent-based approach and rather complex workup. Thus, mechanochemistry was introduced to improve the sustainability and cost/energy-efficiency.[23,24] Synthetic conditions and material/time-cost are summarized and compared in Table S1,† which indicates that the introduction of mechanochemical protocol and optimization of post-synthetic treatment yielded faster synthesis and less sophisticated operation, thus, three times less time and energy consumption.

To assess the effect of various mechanosynthetic procedures on the catalytic activity, three different NaCl-templated (3D) Co–N–C catalysts were synthesized. Procedures involved liquid-assisted grinding (LAG) and compression (LAC) and a combination of both (LAG–LAC). The resulting catalyst materials were designated as **3D-CoNC-LAG**, **3D-CoNC-LAC**, and **3D-CoNC-LAG-LAC**. Nontemplated catalyst **CoNC-LAG** was prepared *via* ball milling for comparative purposes. Upon mechanosynthesis, the reaction mixture changes color from yellow, and the Co-TPTZ complex appears as a pale-red powder, indicating that the TPTZ molecule is coordinated to Co_2^+. The complex formation was also confirmed by the comparative powder X-ray diffraction analysis, where the product pattern did not match any of the starting materials (Fig. S1†).

Microscope pictures (Fig. 2a) demonstrate even integration of micro-sized NaCl crystallites into the framework of the Co-TPTZ complex or the complex evenly surrounding the NaCl crystallites. After the carbonization of NaCl-templated precursors, materials show visible inclusion of NaCl crystallites into the framework of carbon catalysts (Fig. 2c). In contrast, Co-TPTZ-LAG demonstrates a large amount of metallic-Co upon carbonization and appears as dense bulky carbon blocks after acid leaching. In contrast, NaCl-supported catalysts after removing NaCl and acid treatment yielded homogeneous porous carbon materials. This difference after the heat treatment can be attributed to the stabilization effect of NaCl during the pyrolysis, which was previously reported in solution-based syntheses.[23,24] Remarkably, our study indicates that the same effect is maintained in green solid-phase-based mechanosynthesis.

The PXRD analysis also confirms the above-mentioned stabilizing effect. The spectra shown in Fig. 3a are acquired after the carbonization of Co-TPTZ-LAG and Co-TPTZ@NaCl-LAG before the acid leaching. Spectra demonstrate the presence of larger amounts of various Co-particles in non-leached
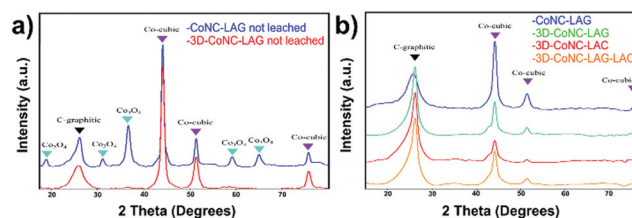

Fig. 3 (a) PXRD pattern of **CoNC-LAG** and **3D-CoNC-LAG** before leaching, (b) PXRD patterns of synthesized catalysts after leaching.
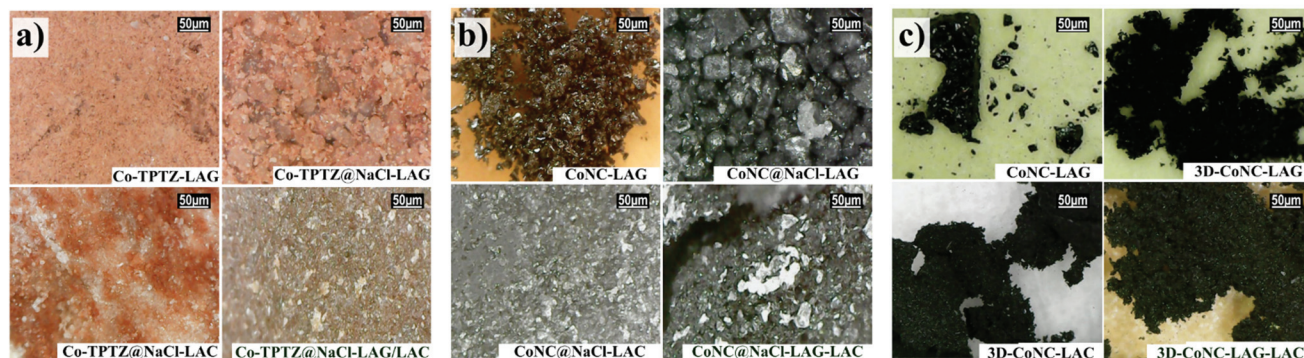

Fig. 2 Microscope pictures of (a) catalyst precursors, (b) non-washed/leached carbonized precursors; (c) CoNC catalysts.

CoNC-LAG (Co-cubic and Co_3O_4) compared to the NaCl-supported carbon material – **3D-CoNC-LAG**, which shows only the peaks attributed to Co-cubic.

Upon the leaching (Fig. 3b), all four products mainly exhibit four strong peaks at 26.5° (graphitic-C) and 44.1°, 51.7°, and 75.9° (Co-cubic), proving that the amount of agglomerated cobalt can be effectively decreased by acid treatment. Furthermore, the pattern of **CoNC-LAG** shows a distinctly higher intensity of metallic-Co, indicating that its amount is higher than in NaCl-supported catalysts. Overall, the decreased formation of Co-particles in NaCl-supported catalysts can be assigned to the template-induced complex stabilization effect during the pyrolysis, as it was described previously.[23,24]

The TEM morphology analyses of prepared materials represented in Fig. 4 support the results of XRD analysis, showing that **CoNC-LAG** visually accommodates more metallic nanoparticles. **CoNC-LAG** appears as a large bulky microscale particle, which serves as another evidence of the agglomeration of catalyst particles and packing of carbon material, resulting in decreased exposure of active sites when carbonized without NaCl crystallites.

On the other hand, the three catalysts, **CoNC-LAG**, **3D-CoNC-LAC**, and **3D-CoNC-LAC**, made by the NaCl-templating method, demonstrate a cross-linked sheet-like structure, which can be seen in their STEM and TEM images (Fig. S2† and Fig. 4). Moreover, the particle size distribution analysis suggests that the average size of the Co-nanoparticles is bigger for **CoNC-LAG** and **3D-CoNC-LAG** (14–16 nm) in comparison to **3D-CoNC-LAC** and **3D-CoNC-LAG-LAC** (12 and 9 nm, respectively). Although small (4–10 nm) Co-nanoparticles can effectively empower OER activity in the produced materials,[41] larger Co particles result in decreased catalytic activity by blocking the pores and hindering the mass transfer.[23,24] HR-TEM images in Fig. S3† demonstrate that Co-nanoparticles are coated with nitrogen-doped carbon forming hollow nanocapsules. The nanocapsule structure of carbon sheets around metallic-Co in combination with meso-/macroporous architecture enhances the mass transport of reactants to the OER/ORR catalytically active sites. Furthermore, carbon sheet layers serve as protection of Co nanoparticles from the electrolyte and agglomeration.[42]

The porosity data collected from the N_2 adsorption–desorption isotherms analysis are summarized in Table 1. The
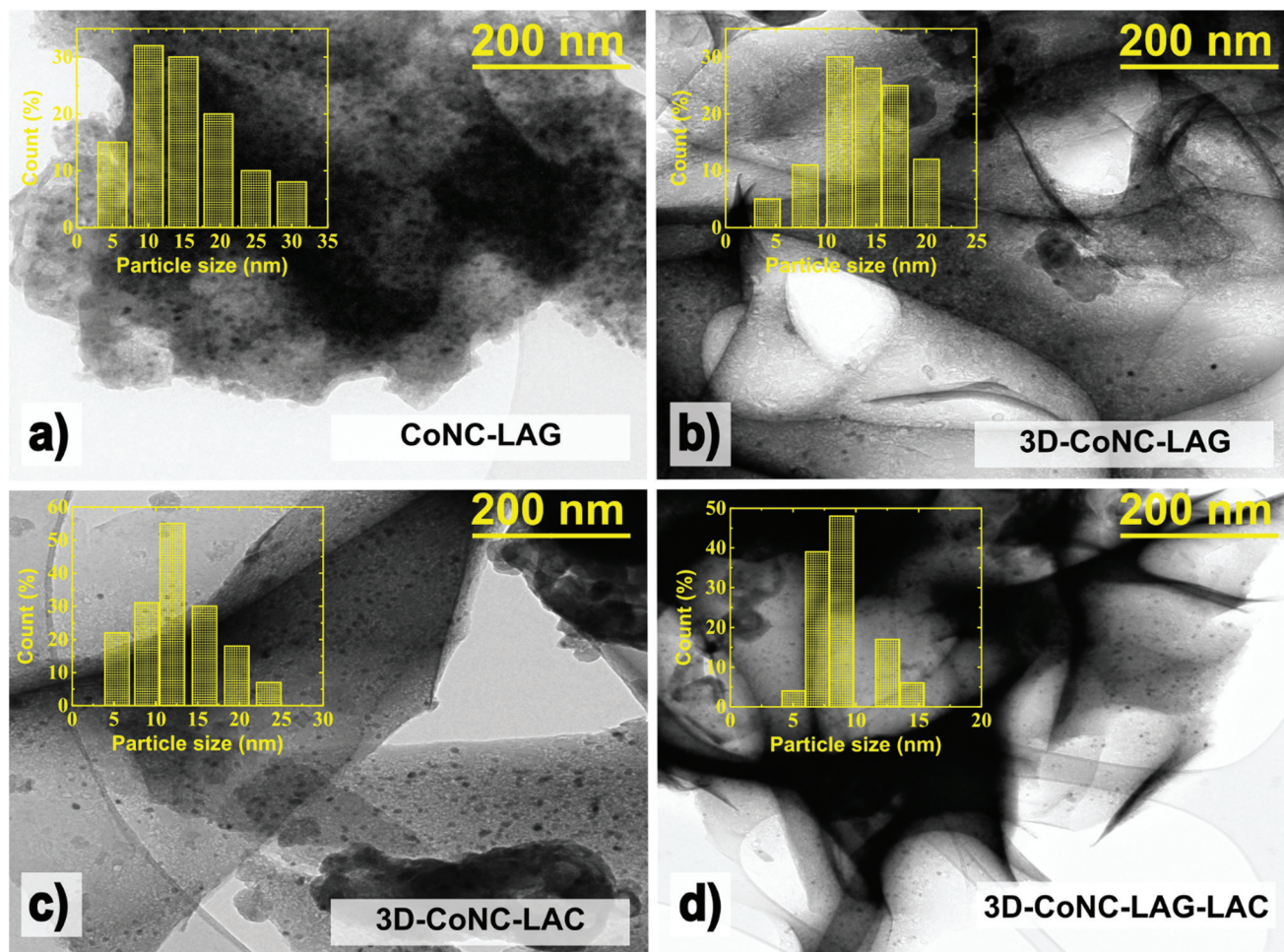

Fig. 4 TEM images and particle size distribution of (a) **CoNC-LAG**, (b) **3D-CoNC-LAG**, (c) **3D-CoNC-LAC**, and (d) **3D-CoNC-LAG-LAC**.

Table 1 Porosity characteristics of the obtained Co–N–C catalysts

Sample	BET surface area ($m^2\ g^{-1}$)	Total pore volume ($cm^3\ g^{-1}$)	Average pore size (nm)
CoNC-LAG	286	0.29	2.0
3D-CoNC-LAG	263	0.25	1.9
3D-CoNC-LAC	490	0.55	2.2
3D-CoNC-LAG-LAC	406	0.45	2.2

CoNC-LAG possesses a slightly higher specific surface area compared to **3D-CoNC-LAG**, 286 and 263 $m^2\ g^{-1}$, respectively. This difference may be attributed to the specifics of the grinding method. It was observed that NaCl-crystallites coverage by Co-TPTZ complex is rather "loose" compared to the compression method; thus, it was hypothesized that not tight enough contact of the complex with the templating agent might reduce the advantageous effects of support. The highest surface area (S_a) was observed with **3D-CoNC-LAC** (490 $m^2\ g^{-1}$), followed by **3D-CoNC-LAG-LAC** (406 $m^2\ g^{-1}$), which can be another indicator of the importance of tight contact of the template with complex. Results of total volume (V_{tot}) calculation correlate with S_a values among the products, with **3D-CoNC-LAC** having the highest total volume (0.55 $cm^3\ g^{-1}$) and **3D-CoNC-LAG** – the lowest ($cm^3\ g^{-1}$). Average pore sizes of **3D-CoNC-LAC** and **3D-CoNC-LAC** are 2.2 nm and **3D-CoNC-LAG** and **CoNC-LAG** – 1.9 and 2.0, accordingly. The pore size distribution graph (Fig. S4†) indicates that all the materials possess a mixed meso- and microporous nature, with the highest peaks in the region of 1–30 nm. The presence of both micropores and mesopores is essential for facilitating the charge transfer and mass transport in the catalytic process.[43]

To analyze the surface elemental composition and presence of catalytically active sites, the XPS technique was utilized. As shown in the survey XPS spectra (Fig. S5†), all produced catalysts mainly contain cobalt, carbon, nitrogen, and oxygen species.

The total surface content of four elements (Co, N, C, and O) in all catalysts is summarized in Table 2. Notably, an examination of the bulk composition of metals in the catalyst materials by MP-AES shows the highest content of cobalt in **CoNC-LAG** (12.35 wt%). This can be explained by lower stability of Co-TPTZ-LAG towards pyrolysis, thus resulting in bulky

Table 2 Elemental composition of catalyst materials determined by XPS and bulk metal composition obtained from MP-AES

Catalyst	Surface elemental composition (at%)				Bulk metal composition (wt%)
	C	N	O	Co	Co
CoNC-LAG	85.9	4.1	7.6	0.8	12.35 ± 0.11
3D-CoNC-LAG	87.0	7.2	5.0	0.5	5.55 ± 0.05
3D-CoNC-LAC	88.8	7.0	4.1	0.5	4.69 ± 0.02
3D-CoNC-LAG-LAC	84.3	9.0	5.0	0.8	5.70 ± 0.04

Co-metal pieces, which are harder to remove by acid treatment; hence these results correlate with previously acquired data.

Deconvoluted high-resolution C 1s photoelectron spectra of all catalyst materials (Fig. S6†) reveal the characteristic peak of sp2 carbon at the binding energy (B.E.) of ~284.3 eV, which can be attributed to C=N bonding and suggests an effective N-atoms doping.[23] N 1s XPS spectra (Fig. 5a) of the obtained catalysts demonstrate the presence of pyridinic (~398.4 eV), graphitic (~400.5 eV), and Co–N_x-type nitrogens (~399.4 eV), which are considered as main contributors to the catalytic activity of the M–N–C type catalysts.[14–17] To check the chemical state of Co atoms, the Co_2p spectra of all catalysts were thoroughly analyzed. (Fig. 5a) Spectra were deconvoluted into three peaks with binding energies of ~779.8, ~781.8, and ~785.6, which can be assigned to the Co–C, Co–N_x, and Co–N_x satellite bonds, respectively.[23]

Content analysis shows that the **3D-CoNC-LAG-LAC** has the highest N/C ratio (10.7%) with a carbon content of 84.32 at% and nitrogen 9.05 at%. Furthermore, the comparison of catalytically active N- and Co-species concentrations (Fig. 5b and c) reveal that the **3D-CoNC-LAG-LAC** has the highest load of pyridinic, pyrrolic, and graphitic-N sites and second-high Co-sites content. These results suggest the efficiency of the combinatorial mechanosynthetic method towards N-atom doping. Both **CoNC-LAG** and **3D-CoNC-LAG-LAC** have the highest Co/C ratio (~0.9%); however, the ratio of metallic-Co is almost twice as big for the NaCl-free catalyst. (7.8% and 4.0%, respectively). Contrarily, the lowest N/C ratio (4.77%) was observed for **CoNC-LAG** with C-content 85.87 at% and N-content – 4.1 at%, and the lowest concentration of active activity N-species, which further proves the positive effect of the NaCl-template method on the efficient N-atom doping. Nevertheless, the concentration of Co–N_x species – one of the major contributors to catalytic activity, in the non-templated catalyst is the highest in the series. (Fig. 5c) Thus, despite the findings, one could still expect a rather high activity towards ORR from this material. Notably, the **3D-CoNC-LAC** demonstrates the lowest concentration of Co–N_x, indicating that the compression technique alone is unable to provide sufficient energy for the effective formation of the Co-TPTZ complex, which further results in Co–N_x species. It was assumed in our study that LAG method, in comparison to LAC, provides higher amount of active Co–N_x species, proving the better complexation reaction efficiency. However, upon the compression of LAG material we observe boost in the concentration of active sites, which can be attributed to an improved stability during the pyrolysis due to the better packing after the compression. The electrochemical assessment of materials is discussed below.

The oxygen electroactivity of prepared Co–N–C catalysts was evaluated by cyclic voltammetry (CV) and rotating disk electrode (RDE) techniques. RDE data (Fig. 6a) demonstrate that **3D-CoNC-LAG-LAC** has the highest ORR activity with an ORR onset potential (E_{on}) value of 0.98 V and a half-wave potential ($E_{1/2}$) value of 0.83 V, which is comparable to the recently reported results for Co–N–C materials (Table S2†). Enhanced ORR electroactivity can be attributed to a highly porous struc-
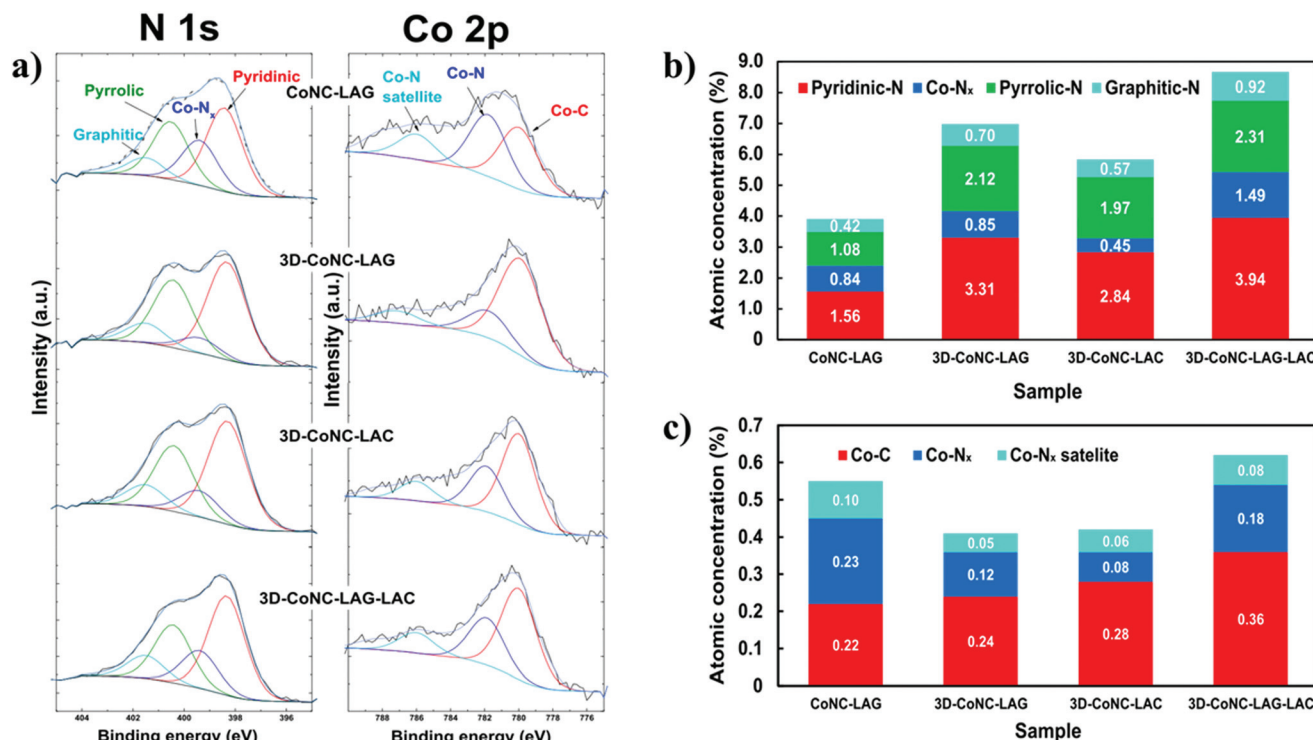
Fig. 5 (a) Deconvoluted high-resolution N 1s and Co 2p photoelectron spectra of Co–N–C catalysts. (b) The content distribution of various nitrogen-rich groups in the prepared catalysts (c) The content distribution of single-atom Co-species in the prepared catalysts.

ture in combination with an abundance of pyridinic-N sites. Template-free catalyst – **CoNC-LAG** showed a second-best result in activity towards ORR, which can be explained by the highest concentration of Co–N$_x$ sites (Fig. 6c). Tafel analysis was performed to get an insight into ORR mechanism (Fig. 6b). Tafel slope values were −61, −59, −37, and −47 mV dec^{-1} for **3D-Co-NC-LAC**, **Co-NC-LAG**, **3D-Co-NC-LAG**, and **3D-Co-NC-LAG–LAC**, demonstrating that the rate determining step of ORR is the transfer of the first electron to the oxygen molecule.

The Koutecky–Levich (K–L) plots constructed from the RDE data in demonstrate good linearity and parallelism (Fig. 6d), indicating first-order reaction kinetics with respect to the dissolved O$_2$ concentration. The electron transfer number calculated from the K–L equation was close to four, indicating that the ORR proceeds to water formation (inset in Fig. 6d).

To further investigate the OER behavior, Co–N–C modified GC electrodes were scanned at 1600 rpm in the potential range of 1–1.8 V vs. RHE (Fig. 6e). The benchmark OER current density of 10 mA cm^{-2} ($E_{j=10}$) was achieved at 1.70 V for **3D-CoNC-LAG-LAC** and resulted in the lowest OER overpotential value ($\eta = 0.46$). Overall bifunctional ORR/OER activity ($\Delta E = E_{j=10} - E_{1/2}$) was calculated, and the lowest ΔE value was acquired for **3D-Co-NC-LAG-LAC**. Kinetic parameters for the obtained catalysts are summarized in Table 3. As discussed above, the OER activity is associated with the presence of Co nanoparticles in the structure of catalysts. The difference in the electrocatalytic efficiency of the materials is the influence

of porosity and the size of Co nanoparticles (CoNPs), where the most electroactive **3D-CoNC-LAG-LAC** has the smallest average size of CoNPs. The above-mentioned results indicate that **3D-CoNC-LAG-LAC** has great bifunctional activity towards ORR and OER.

The stability of the most active **3D-CONC-LAG-LAC** catalyst was investigated employing the chronoamperometry technique, where the fixed potential of the working electrode was held at 0.6 V for ORR and at 1.6 V for OER (Fig. 6f). According to chronoamperometry test results, the ORR current was highly stable during ca. 8 hours of continuous operation. During the OER chronoamperometry measurement, a catalyst exhibited a current decay, which is caused by the production of gas bubbles that partially block the catalyst surface. Nevertheless, after ca. 3000 s the current density attained a stable state and the **3D-CONC-LAG-LAC** catalyst exhibited stable electrocatalytic performance towards OER. The promising results of the proposed mechanosynthetic methodology show that high-performing PGM-free catalysts can be produced in an inexpensive and sustainable way. The data summarized in Table S2† shows that the catalysts produced in our study possess compatible activity, however the comparative data in Table S3† shows that the proposed methodology has several major advantages: minimal amount of non-toxic solvent, short total reaction time, and easy-to-conduct protocols. These benefits in turn result in lower-to-none toxic waste and considerably less time and energy consumption. This study is dedicated to bringing the global goal closer to reality: a cheap,
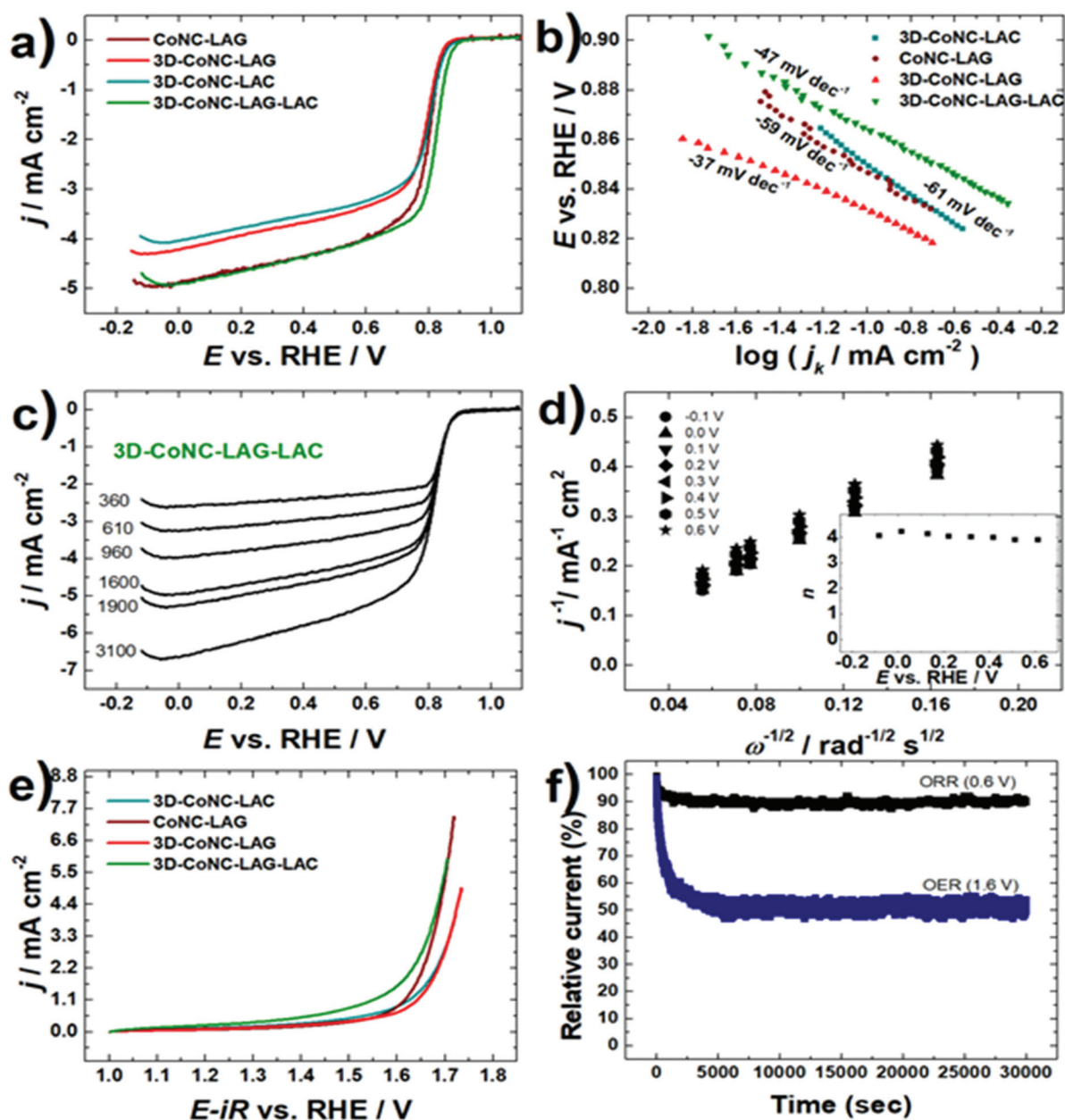
Fig. 6 (a) ORR polarization curves obtained for all catalyst materials in O_2-saturated 0.1 M KOH at 1600 rpm; (b) Tafel plots constructed from the RDE data; (c) ORR polarization curves recorded for **3D-CoNC-LAG-LAC** at different electrode rotation rates; (d) Koutecky−Levich plots obtained for **3D-CoNC-LAG-LAC** modified GC electrode (Inset: number of electrons transferred per O_2 molecule); (e) OER polarization curves recorded in Ar-saturated 0.1 M KOH; $\nu = 10$ mV s^{-1}. (f) Chronoamperometric response for **3D-CoNC-LAG-LAC** recorded at an applied potential of 0.6 V for ORR and 1.6 V for OER.

completely PGM-free catalyst-based fuel cell system with high performance and long life.

Conclusions

In this work we present a novel green and cost-effective method for producing M–N–C-type catalysts with excellent bifunctional oxygen electroactivity. The suggested method is based on the application of mechanochemistry in the form of

Table 3 Kinetic parameters of ORR and OER obtained from RDE data

Sample	$E_{1/2}$ (V)	E_{onset} (V)	n	$E_{j=10}$ (V)	η_{OER} (V)	ΔE (V)
CoNC-LAG	0.79	0.96	3.1	1.73	0.49	0.94
3D-CoNC-LAG	0.78	0.92	3.4	1.80	0.56	1.04
3D-CoNC-LAC	0.79	0.94	3.5	1.80	0.56	1.01
3D-CoNC-LAG-LAC	0.83	0.98	4.0	1.70	0.46	0.87

liquid-assisted grinding and compression. The current study yielded a series of meso/microporous Co and N doped carbon materials as a highly active and stable oxygen electrocatalyst. Porosity, electrocatalytic activity, and stability of materials were improved by applying the NaCl sacrificial template. This research confirms the efficiency of the mechanochemical approach towards catalyst production, indicating that the advantageous effect of NaCl-template is also maintained. The excellent ORR/OER performance can be attributed to the conventional active sites, including Co–N$_x$ moieties, whose presence was confirmed by XPS analysis. A relatively large surface area is also suggested to be a contributor facilitating mass transport.

A proposed method opens new avenues for environmentally sustainable large-scale implementation of high-performance M–N–C catalysts for clean energy systems. This low-cost and facile method may empower the switch to Pt-free electrocatalysts for ORR in fuel cells.

Author contributions

A. K. conceived the concept and experiments design, fabricated the catalysts, wrote the manuscript. G. Y. performed the material electrochemical characterization and analyzed the data. K. Š. performed the electron microscopy imaging. J. A. performed PXRD. J. L. and M. K. together performed N$_2$ physisorption analysis. P. P. performed MP-AES experiments. A. K. and V. K. together performed XPS analysis. A. K and N. K. were the primary writers of the manuscript. N. K. supervised the research. All authors discussed the results and commented on the manuscript.

Conflicts of interest

There are no conflicts to declare.

Acknowledgements

References

1 Y. Li, W. Zhou, H. Wang, L. Xie, Y. Liang, F. Wei, J.-C. Idrobo, S. J. Pennycook and H. Dai, *Nat. Nanotechnol.*, 2012, **7**, 394–400.

2 V. Das, *Renewable Sustainable Energy Rev.*, 2017, 9.

3 Z. Wu, X. F. Lu, S. Zang and X. W. Lou, *Adv. Funct. Mater.*, 2020, **30**, 1910274.

4 T. J. Omasta, Y. Zhang, A. M. Park, X. Peng, B. Pivovar, J. R. Varcoe and W. E. Mustain, *J. Electrochem. Soc.*, 2018, **165**, F710–F717.

5 M. Li, X. Bi, R. Wang, Y. Li, G. Jiang, L. Li, C. Zhong, Z. Chen and J. Lu, *Matter*, 2020, **2**, 32–49.

6 H. A. Miller and F. Vizza, *Anion Exchange Membrane Fuel Cells: Principles, Materials and Systems*, Springer, 1st edn., 2018, vol. 63.

7 Z.-C. Yao, T. Tang, J.-S. Hu and L.-J. Wan, *Energy Fuels*, 2021, **35**, 6380–6401.

8 M. D. Bhatt and J. Y. Lee, *Energy Fuels*, 2020, **34**, 6634–6695.

9 J. Wang, L. Gan, W. Zhang, Y. Peng, H. Yu, Q. Yan, X. Xia and X. Wang, *Sci. Adv.*, 2018, **4**, 7970.

10 X. Fu, P. Zamani, J.-Y. Choi, F. M. Hassan, G. Jiang, D. C. Higgins, Y. Zhang, M. A. Hoque and Z. Chen, *Adv. Mater.*, 2017, **29**, 1604456.

11 X.-F. Lu, L.-F. Gu, J.-W. Wang, J.-X. Wu, P.-Q. Liao and G.-R. Li, *Adv. Mater.*, 2017, **29**, 1604437.

12 P. Song, M. Luo, X. Liu, W. Xing, W. Xu, Z. Jiang and L. Gu, *Adv. Funct. Mater.*, 2017, **27**, 1700802.

13 X. F. Lu, Y. Chen, S. Wang, S. Gao and X. W. Lou, *Adv. Mater.*, 2019, **31**, 1902339.

14 P. Song, Y. Wang, J. Pan, W. Xu and L. Zhuang, *J. Power Sources*, 2015, **300**, 279–284.

15 L. Osmieri, A. H. A. Monteverde Videla and S. Specchia, *J. Power Sources*, 2015, **278**, 296–307.

16 F. Roncaroli, E. S. Dal Molin, F. A. Viva, M. M. Bruno and E. B. Halac, *Electrochim. Acta*, 2015, **174**, 66–77.

17 R. Othman, Md. S. Hossain and N. H. Jabarullah, *Appl. Organomet. Chem.*, 2017, **31**, 3738.

18 K. Zhang and R. Zou, *Small*, 2021, **17**, 2100129.

19 P. Munnik, P. E. de Jongh and K. P. de Jong, *Chem. Rev.*, 2015, **115**, 6687–6718.

20 J. Pampel and T.-P. Fellinger, *Adv. Energy Mater.*, 2016, **6**, 1502389.

21 J. Pampel, A. Mehmood, M. Antonietti and T.-P. Fellinger, *Mater. Horiz.*, 2017, **4**, 493–501.

22 W. Ding, Z. Wei, S. Chen, X. Qi, T. Yang, J. Hu, D. Wang, L.-J. Wan, S. F. Alvi and L. Li, *Angew. Chem., Int. Ed.*, 2013, **52**, 11755–11759.

23 C. Guo, R. Zhou, Z. Li, Y. Si, W. Liao, W. Sun, S. Xiang, X. Luo, M. Luo and Z. Luo, *Microporous Mesoporous Mater.*, 2020, **303**, 110281.

24 C. Guo, Y. Li, W. Liao, Y. Liu, Z. Li, L. Sun, C. Chen, J. Zhang, Y. Si and L. Li, *J. Mater. Chem. A*, 2018, **6**, 13050–13061.

25 J. Cao, Z. Chen, J. Xu, W. Wang and Z. Chen, *Electrochim. Acta*, 2013, **88**, 184–192.

26 R. Wu, J. Wang, K. Chen, S. Chen, J. Li, Q. Wang, Y. Nie, Y. Song, H. Chen and Z. Wei, *Electrochim. Acta*, 2017, **244**, 47–53.

27 H. Adabi, A. Shakouri, N. Ul Hassan, J. R. Varcoe, B. Zulevi, A. Serov, J. R. Regalbuto and W. E. Mustain, *Nat. Energy*, 2021, **6**, 834–843.

28 A. P. Amrute, J. De Bellis, M. Felderhoff and F. Schüth, *Chem. – Eur. J.*, 2021, **27**, 6819–6847.

29 S. L. James, C. J. Adams, C. Bolm, D. Braga, P. Collier, T. Friščić, F. Grepioni, K. D. M. Harris, G. Hyett, W. Jones, A. Krebs, J. Mack, L. Maini, A. G. Orpen, I. P. Parkin, W. C. Shearouse, J. W. Steed and D. C. Waddell, *Chem. Soc. Rev.*, 2012, **41**, 413–447.

30 T. Friščić, *Encyclopedia of Inorganic and Bioinorganic Chemistry*, ed. R. A. Scott, John Wiley & Sons, Ltd, Chichester, UK, 2014, pp. 1–19.

31 D. Chen, J. Zhao, P. Zhang and S. Dai, *Polyhedron*, 2019, **162**, 59–64.

32 T. Friščić and L. Fábián, *CrystEngComm*, 2009, **11**, 743.

33 L. Paseta, G. Potier, S. Sorribas and J. Coronas, *ACS Sustainable Chem. Eng.*, 2016, **7**, 3780–3785.

34 B. G. Fiss, N.-N. Vu, G. Douglas, T.-O. Do, T. Friščić and A. Moores, *ACS Sustainable Chem. Eng.*, 2020, **8**, 12014–12024.

35 D. E. Crawford, C. K. G. Miskimmin, A. B. Albadarin, G. Walker and S. L. James, *Green Chem.*, 2017, **19**, 1507–1518.

36 P. Baláž, M. Achimovičová, M. Baláž, P. Billik, Z. Cherkezova-Zheleva, J. M. Criado, F. Delogu, E. Dutková, E. Gaffet, F. J. Gotor, R. Kumar, I. Mitov, T. Rojac, M. Senna, A. Streletskii and K. Wieczorek-Ciurowa, *Chem. Soc. Rev.*, 2013, **42**, 7571.

37 R. A. Buyanov, V. V. Molchanov and V. V. Boldyrev, *Catal. Today*, 2009, **144**, 212–218.

38 J. Tian, A. Morozan, M. T. Sougrati, M. Lefèvre, R. Chenitz, J.-P. Dodelet, D. Jones and F. Jaouen, *Angew. Chem., Int. Ed.*, 2013, **52**, 6867–6870.

39 L. Osmieri, A. H. A. Monteverde Videla and S. Specchia, *J. Solid State Electrochem.*, 2016, **20**, 3507–3523.

40 V. Chipakwe, P. Semsari, T. Karlkvist, J. Rosenkranz and S. C. Chelgani, *J. Mater. Res. Technol.*, 2020, **9**, 8148–8162.

41 E. Locke, S. Jiang and S. K. Beaumont, *Top. Catal.*, 2018, **61**, 977–985.

42 Y. Zhang, P. Wang, J. Yang, S. Lu, K. Li, G. Liu, Y. Duan and J. Qiu, *Carbon*, 2021, **177**, 344–356.

43 H.-W. Liang, X. Zhuang, S. Brüller, X. Feng and K. Müllen, *Nat. Commun.*, 2014, **5**, 4973.